Influence functions of a thin shallow meniscus-shaped mirror

Luc Arnold

Thin shallow spherical shell theory is used to derive the general influence function, owing to uniform and/or discrete (actuators) loads, for a thin shallow meniscus-shaped mirror of uniform thickness with a central hole and supported at discrete points. Small elastic deformations are considered. No symmetry on the load distribution constrains the model. Explicit analytical expressions of the set of equations are given for calculating the influence functions. Results agree with the finite element analysis (FEA) to within 1%. When the FEA requires megabytes of RAM memory, the analytical method needs only kilobytes and typically runs 30 times faster. This is a crucial advantage for the iterative optimization of mirror supports such as large passive or active meniscus-shaped primary mirror supports or Cassegrain/Gregorian adaptive secondary actuator configurations. References are given on estimating the shear effects (thick mirror), the thickness variation effect, and the influence of the size of the support pads. © 1997 Optical Society of America

Key words: Telescope mirrors, mirror deformations, active optics, influence functions, meniscus-shaped mirrors.

1. Introduction

The finite element analysis[1] (FEA) is the classic numerical method used to calculate the deformations of telescope mirrors, i.e., the influence functions (IF's), owing to gravitational or actuator loadings. The FEA generally requires large computer resources. Because telescope mirrors are often of simple geometry, i.e., annular with a constant thickness, these elastic deformations can also be described in an analytical form by using a thin shallow spherical shell theory[2–9] for a thin shallow meniscus-shaped mirror or for a flat mirror, the plate-bending theory.[6,10] Such analytical solutions allow rapid estimations of mirror deformations, which are convenient for passive or active support optimization iterative processes.[9,11–13] This kind of calculation concerns either passive or active primary mirrors or adaptive Cassegrain or Gregorian secondaries. The duration of parametric studies also becomes reasonable.

The deformations under uniform loading, the so-called uniform load influence function (ULIF), the deformation under gravitational loading, the socalled gravity influence function (GIF), and the deformation under discrete forces, the socalled actuator influence function (AIF), for a flat mirror (infinite radius of curvature) have been given in previous papers.[9,11,13,14]

2. Definitions of an Applicability of the Theory

Here a thin shallow meniscus-shaped mirror of constant thickness h is considered (Fig. 1). The mirror is thin if

$$h/\bar{u} \leq \sim 1/15, \tag{1}$$

where $\bar{u}$ is the typical span between the supports. The effects of shear stresses across the thickness are neglected in the following theory. Studies of shear effects in thick mirrors are described in Refs. 7, 9, 11, 15, and 16 and are based on the Reissner theory.[6,17,18] Several authors also describe a semianalytical method to take into account an axisymmetric thickness variation.[9,16,19] According to the assumption of thinness, mirror optical, middle, and rear surfaces are considered to be the same.

The meniscus-shaped mirror is shallow if its sag is small compared with its diameter $2a$ or quantita-

The author is with the Laboratoire d'Astrophysique Observationnelle, Collège de France et Observatoire de Haute Provence, Centre National de la Recherche Scientifique, F-04 870 Saint Michel l'Observatoire, France.

Received 30 April 1996; revised manuscript received 3 September 1996.

0003-6935/97/102019-10$10.00/0

© 1997 Optical Society of America

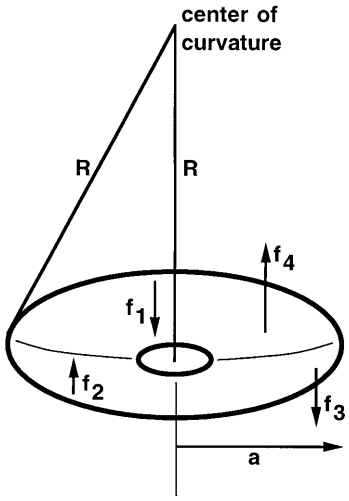

Fig. 1. Thin shallow meniscus-shaped mirror with a central hole: R, radius of curvature; a, mirror outer radius. In this example, four discrete axial forces f_j are applied to the mirror. Three of them (f_1, f_2, f_3) are arranged with a threefold symmetry.

tively[2,5,9]

$$\frac{R}{2a} \gg 1, \tag{2}$$

where R is the mirror radius of curvature (Fig.1). Such a mirror shape is common today in the design of a large optical telescope because it meets the specifications of (1) a small focal ratio of the primary mirror (<2, inducing a strongly curved optical surface) and (2) a lightweight (primary or secondary) mirror. According to the assumption of shallowness, it is irrelevant whether the forces are applied parallel to the mirror axis (axial forces) or toward the mirror center of curvature. Note also that with the assumptions of shallowness and thinness, there is no difference, apart from a factor, between the GIF and the ULIF.

In the theory below only small elastic deformations w defined as

$$w \ll h \tag{3}$$

are considered.

The mirror is supported at discrete points. No symmetry is assumed in the applied load distribution, which includes only axial loads (Fig. 1).

Noethe[8] used shallow spherical shell natural modes to describe the IF of the Very Large Telescope 8-m mirrors. The IF is therefore an infinite linear combination of these modes.

The direct method proposed here is derived from the two fundamental equations of equilibrium of a thin shallow spherical shell. The methodology is similar to that used for flat mirrors, but the nature of the analytical solutions is different and the number of equations to be solved is larger. Here the load distribution and the IF are described by a Fourier series. Again an infinite number of Fourier modes is necessary to describe the IF, but in practice the addition of the first 15 nonzero modes is sufficient for optical purposes. In Section 5, I briefly discuss when shell theory must be used rather than plate theory.

3. General Form of the Influence Functions

A circular horizontal thin shallow meniscus-shaped mirror with a central hole of radius c is considered. The mirror material is characterized by its Young's modulus E and its Poisson's ratio ν.

The mirror is in static equilibrium between a force P, resulting from a uniform loading (typically its weight) and a set of k concentrated axial forces (Fig. 1). The polar coordinates of the k forces f_j are $r = b_j$ and $\theta = \theta_j$ and are measured from the mirror apex.

The thin shallow shell theory[2–6,8,9] leads to two fundamental equations:

$$\nabla^2\nabla^2 F + \frac{hE}{R}\nabla^2 w = -(1-\nu)\nabla^2\Omega, \tag{4}$$

$$D\nabla^2\nabla^2 w - \frac{1}{R}\nabla^2 F = q + \frac{2\Omega}{R}, \tag{5}$$

from which the IF w, i.e., the deformation normal to the mirror surface, must be derived. The second unknown F is a stress function. The symbol ∇^2 is the Laplacian operator:

$$\nabla^2 = \frac{\partial^2}{\partial r^2} + \frac{1}{r}\frac{\partial}{\partial r} + \frac{1}{r^2}\frac{\partial^2}{\partial \theta^2}, \tag{6}$$

and D is the flexural rigidity:

$$D = \frac{Eh^3}{12(1-\nu^2)}. \tag{7}$$

In Eqs. (4) and (5), Ω is the potential of assumed conservative in-plane load distributions.[2–6,8,9] The load, $q = q(r, \theta)$, per unit area represents the normal load distribution applied to the mirror. Note that if the radius of curvature R is infinite, Eq. (5) becomes $D\nabla^2\nabla^2 w = q$, which is the well-known equation from the thin-plate-bending theory.

With the two-dimensional Dirac δ function verifying

$$\iint \frac{1}{b_j}\delta(r-b_j)\delta(\theta-\theta_j) r\,dr\,d\theta = 1, \tag{8}$$

the load q is given by

$$q(r,\theta) = \frac{-P}{\pi(a^2-c^2)} + \sum_{j=1}^{k}\frac{f_j}{b_j}\delta(r-b_j)\delta(\theta-\theta_j) \tag{9}$$

or

$$q(r,\theta) = \frac{-P}{\pi(a^2-c^2)} + \sum_{j=1}^{k}\frac{f_j}{2\pi b_j}\delta(r-b_j) \times \sum_{m=-\infty}^{\infty}\exp[im(\theta-\theta_j)], \tag{10}$$

where the Dirac function $\delta(\theta-\theta_j)$ has been replaced by its complex Fourier series. Here the Dirac func-

tion shows that it is assumed that the diameter of the support pads is negligible with respect to the mirror outer radius. A method to take into account the finite size of the pads is given in Refs. 12 and 13.

If the mirror weight is balanced by k discrete supports placed on a single concentric ring (radius, b) with a k-fold symmetry, each support carrying a fraction $1/k$ of the weight, the load q can then be written as

$$q(r, \theta) = \frac{-P}{\pi(a^2 - c^2)} + \frac{P}{k}\frac{\delta(r-b)}{b}\sum_{j=1}^{k}\delta\left(\theta - \frac{2j\pi}{k} - \theta_0\right), \tag{11}$$

where θ_0 is the azimuth of the supports with respect to the origin axis. The term

$$\sum_{j=1}^{k}\delta\left(\theta - \frac{2j\pi}{k} - \theta_0\right)$$

can also be written as a complex Fourier series. The load can thus be rewritten in the convenient form

$$q(r, \theta) = \frac{-P}{\pi(a^2 - c^2)} + \frac{P\delta(r-b)}{2\pi b} + \frac{P\delta(r-b)}{\pi b}\sum_{n=1}^{\infty}\cos[kn(\theta - \theta_0)]. \tag{12}$$

Because rotational symmetry $m = kn > 1$, this kind of load does not contain harmonics with $m = 1$.

The Fourier series, Eq. (10), suggests solving for a Fourier series for w and F of the form

$$[w(r, \theta), F(r, \theta)] = \sum_{m=-\infty}^{\infty}[w_m(r), F_m(r)]\exp im\theta. \tag{13}$$

The general solution for the radial functions, $w_m(r)$ and $F_m(r)$, of the homogeneous system associated with Eqs. (4) and (5) are for $m = 0$ (Refs. 3–7, 9):

$$w_0 = C_1 ber_0 x + C_2 bei_0 x + C_3 ker_0 x + C_4 kei_0 x + C_5, \tag{14}$$

$$F_0 = \frac{Eh^2}{[12(1-\nu^2)]^{1/2}}(C_1 bei_0 x - C_2 ber_0 x + C_3 kei_0 x - C_4 ker_0 x + C_6 \ln x + C_8), \tag{15}$$

and for $|m| \geq 1$ (Refs. 5 and 9)

$$w_m = C_1 x^m + C_3 x^{-m} + C_5 ber_m x + C_6 bei_m x + C_7 ker_m x + C_8 kei_m x, \tag{16}$$

$$F_m = \frac{Eh^2}{[12(1-\nu^2)]^{1/2}}(C_2 x^m + C_4 x^{-m} + C_5 bei_m x - C_6 ber_m x + C_7 kei_m x - C_8 ker_m x). \tag{17}$$

Constants $C_1, \ldots, C_8$ characterize w_m and F_m. The functions bei_0, ber_0, kei_0, ker_0, bei_m, ber_m, kei_m, and ker_m are the Kelvin functions.[20] The argument x is defined by

$$x = \frac{r}{l} = \frac{[12(1-\nu^2)]^{1/4}}{\sqrt{Rh}}r. \tag{18}$$

One particular solution for w and F must be found and added to Eqs. (14)–(17) to obtain the complete solution of the system of Eqs. (4) and (5). This research has been carried out by several authors[3,5–7,9] for $m = 0$. They give explicit analytical expressions of w_0 and F_0 or at least describe a method for calculating them. Reissner[4] also considered the case $m = 1$ and gave solutions in some specific applications.

Here only the general method for calculating $w_{|m|\geq 1}$ and $F_{|m|\geq 1}$ is given.

On a technical point, constants $C_1, \ldots, C_8$ are calculated for the positive value of the integer m, and the final deflection for a given harmonic is the real part noted $w_{m\geq 1}(r, \theta)$ of the complex value $\tilde{w}_{m\geq 1}(r)$ according to

$$w_{m\geq 1}(r, \theta) = \mathrm{Re}[2 \times \tilde{w}_{m\geq 1}(r) \times \exp im\theta], \tag{19}$$

where $\tilde{w}_{m\geq 1}(r)$ is a complex function of θ_j and b_j through the constants C_i.

4. Derivation of the Influence Functions for Harmonics, $m \geq 1$

With Eq. (10) and for a given harmonic, $m \geq 1$, Eqs. (4) and (5) become

$$\nabla^2\nabla^2 F_m + \frac{hE}{R}\nabla^2 w_m = 0, \tag{20}$$

$$D\nabla^2\nabla^2 w_m - \frac{1}{R}\nabla^2 F_m = \sum_{j=1}^{k}\frac{f_j}{2\pi b_j}\delta(r - b_j)\exp(-im\theta_j). \tag{21}$$

Thus, as soon as $r \neq b_j$, the system becomes homogeneous. Because the second right-hand member involves Dirac functions, the particular solutions are system Green's functions.[21] But it is not necessary to solve them. To calculate constants C_i, one has to consider only the general solutions, Eqs. (16) and (17), and to take into account the discontinuities of the transverse forces caused by the discrete forces at $r = b_j$ in appropriate jump relations, as shown below.

A. Edge Conditions

The mirror is assumed to satisfy the free edge boundary conditions. Therefore the conditions at the inner and the outer edges are[8,9,22]

$$N_{r4}(r = c) = N_r(r = a) = 0, \quad N_{r\theta}(r = c) = N_{r\theta}(r = a) = 0,$$
$$M_r(r = c) = M_r(r = a) = 0, \quad V_r(r = c) = V_r(r = a) = 0, \tag{22}$$

where V_r is a resulting transverse force parallel to the optical axis and defined by

$$V_r = Q_r + \frac{1}{r}\frac{\partial M_{r\theta}}{\partial\theta} - \frac{r}{R}N_r. \tag{23}$$

M_r is the bending moment, $M_{r\theta}$ is the twisting moment, Q_r is the resulting force perpendicular to the mirror surface, and N_r and $N_{r\theta}$ are the direct stress and the tangential shearing stress resulting in the plane of the mirror surface, respectively. Their expressions versus w and F are[6,8–11,14,22]

$$N_r = \frac{1}{r}\frac{\partial F}{\partial r} + \frac{1}{r^2}\frac{\partial^2 F}{\partial \theta^2} + \Omega, \tag{24}$$

$$N_{r\theta} = -\frac{\partial}{\partial r}\left(\frac{1}{r}\frac{\partial F}{\partial \theta}\right), \tag{25}$$

$$M_r = -D\left[\frac{\partial^2 w}{\partial r^2} + \nu\left(\frac{1}{r}\frac{\partial w}{\partial r} + \frac{1}{r^2}\frac{\partial^2 w}{\partial \theta^2}\right)\right], \tag{26}$$

$$M_{r\theta} = -(1-\nu)D\frac{\partial}{\partial r}\left(\frac{1}{r}\frac{\partial w}{\partial \theta}\right), \tag{27}$$

$$Q_r = -D\frac{\partial \nabla^2 w}{\partial r}. \tag{28}$$

B. Harmonics, $m > 1$

If k supports (or actuators) have distinct radii b_j, they form $k + 1$ concentric annular surfaces, and for a given value of m, $8(k + 1)$ constants $C_1, \ldots, C_8$ must be determined to calculate w_m. $C_1, \ldots, C_8$ are derived from $8 \times k$ conditions at $r = b_j$ and the 2×4 edge conditions at the inner and the outer edges. The explicit analytical form of this set of equations is the following (the symbols $'$ and $''$ denote the first and second derivative, respectively, with respect to variable r, except for the Kelvin functions where the derivatives are with respect to variable x):

- Edge conditions: four equations at $r = c$ and four equations at $r = a$ [Eq. (22)].

The two equations for N_r and $N_{r\theta}$ at $r = a$ are, respectively,

$$aF_m'(a) - m^2 F_m(a) = 0, \tag{29}$$

$$m[aF_m'(a) - F_m(a)] = 0. \tag{30}$$

They can be simplified and rewritten as

$$F_m(a) = 0, \qquad F_m'(a) = 0, \tag{31}$$

or, respectively, as

$$\begin{aligned} &C_2 x_a{}^m + C_4 x_a{}^{-m} + C_5 bei_m x_a - C_6 ber_m x_a \\ &\qquad + C_7 kei_m x_a - C_8 ker_m x_a = 0, \\ &C_2 m x_a{}^{m-1} - C_4 m x_a{}^{-m-1} + C_5 bei_m' x_a - C_6 ber_m' x_a \\ &\qquad + C_7 kei_m' x_a - C_8 ker_m' x_a = 0, \end{aligned} \tag{32}$$

where

$$x_a = a/l. \tag{33}$$

The two other edge conditions, $M_r = 0$ and $V_r = 0$ [Eq. (22)], are, respectively,

$$w_m''(a) + \frac{\nu}{a} w_m'(a) - \nu\frac{m^2}{a^2} w_m(a) = 0, \tag{34}$$

$$-\frac{\partial \nabla^2 w_m}{\partial r} + (1-\nu)m^2\left(\frac{w_m'}{r^2} - \frac{w_m}{r^3}\right) = 0, \tag{35}$$

or, respectively,

$$\begin{aligned} 0 = {} & C_1(1-\nu)m(m-1)x_a{}^{m-2} + C_3(1-\nu)m(m+1)x_a{}^{-m-2} \\ & + C_5\left[-bei_m x_a - (1-\nu)\left(\frac{ber_m' x_a}{x_a} - \frac{m^2 ber_m x_a}{x_a{}^2}\right)\right] \\ & + C_6\left[ber_m x_a - (1-\nu)\left(\frac{bei_m' x_a}{x_a} - \frac{m^2 bei_m x_a}{x_a{}^2}\right)\right] \\ & + C_7\left[-kei_m x_a - (1-\nu)\left(\frac{ker_m' x_a}{x_a} - \frac{m^2 ker_m x_a}{x_a{}^2}\right)\right] \\ & + C_8\left[ker_m x_a - (1-\nu)\left(\frac{kei_m' x_a}{x_a} - \frac{m^2 kei_m x_a}{x_a{}^2}\right)\right], \end{aligned} \tag{36}$$

$$\begin{aligned} 0 = {} & C_1(1-\nu)m^2(m-1)x_a{}^{m-3} - C_3(1-\nu) \\ & \times m^2(m+1)x_a{}^{-m-3} \\ & + C_5\left[bei_m' x_a + (1-\nu)m^2\left(\frac{ber_m' x_a}{x_a{}^2} - \frac{ber_m x_a}{x_a{}^3}\right)\right] \\ & + C_6\left[-ber_m' x_a + (1-\nu)m^2\left(\frac{bei_m' x_a}{x_a{}^2} - \frac{bei_m x_a}{x_a{}^3}\right)\right] \\ & + C_7\left[kei_m' x_a + (1-\nu)m^2\left(\frac{ker_m' x_a}{x_a{}^2} - \frac{ker_m x_a}{x_a{}^3}\right)\right] \\ & + C_8\left[-ker_m' x_a + (1-\nu)m^2\left(\frac{kei_m' x_a}{x_a{}^2} - \frac{kei_m x_a}{x_a{}^3}\right)\right]. \end{aligned} \tag{37}$$

Let us note now that

$$\Delta_j C_i = \lim_{r \to b_j{}^+} C_i - \lim_{r \to b_j{}^-} C_i. \tag{38}$$

- w_m is continuous at a support radius of $r = b_j$:

$$\lim_{r \to b_j{}^+} w_m = \lim_{r \to b_j{}^-} w_m, \tag{39}$$

which, with Eq. (16) and $x_{b_j} = b_j/l$, leads to

$$\begin{aligned} \Delta_j C_1 x_{b_j}{}^m + \Delta_j C_3 x_{b_j}{}^{-m} + \Delta_j C_5 ber_m x_{b_j} + \Delta_j C_6 bei_m x_{b_j} \\ + \Delta_j C_7 ker_m x_{b_j} + \Delta_j C_8 kei_m x_{b_j} = 0. \end{aligned} \tag{40}$$

- dw_m/dr is continuous at support radius $r = b_j$:

$$\lim_{r \to b_j{}^+} \frac{\partial w_m}{\partial r} = \lim_{r \to b_j{}^-} \frac{\partial w_m}{\partial r}, \tag{41}$$

and, again with Eq. (16), we obtain

$$\Delta_j C_1 m {x_{b_j}}^{m-1} - \Delta_j C_3 m {x_{b_j}}^{-m-1} + \Delta_j C_5 ber_m' x_{b_j} + \Delta_j C_6 bei_m' x_{b_j} + \Delta_j C_7 ker_m' x_{b_j} + \Delta_j C_8 kei_m' x_{b_j} = 0. \quad (42)$$

- $d^2 w_m/dr^2$ (or M_r) is continuous at support radius $r = b_j$:

$$\lim_{r \to b_j^+} \frac{\partial^2 w_m}{\partial r^2} = \lim_{r \to b_j^-} \frac{\partial^2 w_m}{\partial r^2}, \quad (43)$$

and, once more with Eq. (16), we obtain

$$\Delta_j C_1 m(m-1) {x_{b_j}}^{m-2} + \Delta_j C_3 m(m+1) {x_{b_j}}^{-m-2} + \Delta_j C_5 ber_m'' x_{b_j} + \Delta_j C_6 bei_m'' x_{b_j} + \Delta_j C_7 ker_m'' x_{b_j} + \Delta_j C_8 kei_m'' x_{b_j} = 0. \quad (44)$$

- The meridional displacement[5,9] v_m (see Appendix A) is also continuous at support radius $r = b_j$:

$$\Delta_j C_1 \frac{{x_{b_j}}^{m+1}}{m+1} - \Delta_j C_2(1+\nu) m {x_{b_j}}^{m-1} - \Delta_j C_3 \frac{{x_{b_j}}^{-m+1}}{m-1} + \Delta_j C_4(1+\nu) m {x_{b_j}}^{-m-1} - \Delta_j C_5(1+\nu) bei_m' x_{b_j} + \Delta_j C_6(1+\nu) ber_m' x_{b_j} - \Delta_j C_7(1+\nu) kei_m' x_{b_j} + \Delta_j C_8(1+\nu) ker_m' x_{b_j} = 0. \quad (45)$$

- dv_m/dr is continuous at support radius $r = b_j$:

$$\Delta_j C_1 {x_{b_j}}^{m} - \Delta_j C_2(1+\nu) m(m-1) {x_{b_j}}^{m-2} + \Delta_j C_3 {x_{b_j}}^{-m} - \Delta_j C_4(1+\nu) m(m+1) {x_{b_j}}^{-m-2} - \Delta_j C_5(1+\nu) bei_m'' x_{b_j} + \Delta_j C_6(1+\nu) ber_m'' x_{b_j} - \Delta_j C_7(1+\nu) kei_m'' x_{b_j} + \Delta_j C_8(1+\nu) ker_m'' x_{b_j} = 0. \quad (46)$$

- The circumferential displacement[5,9] u_m (see Appendix B) is also continuous at support radius $r = b_j$:

$$\Delta_j C_1 \frac{{x_{b_j}}^{m+1}}{m+1} + \Delta_j C_2(1+\nu) m {x_{b_j}}^{m-1} + \Delta_j C_3 \frac{{x_{b_j}}^{-m+1}}{m-1} + \Delta_j C_4(1+\nu) m {x_{b_j}}^{-m-1} + \Delta_j C_5(1+\nu) \frac{bei_m x_{b_j}}{x_{b_j}} - \Delta_j C_6(1+\nu) \frac{ber_m x_{b_j}}{x_{b_j}} + \Delta_j C_7(1+\nu) \frac{kei_m x_{b_j}}{x_{b_j}} - \Delta_j C_8(1+\nu) \frac{ker_m x_{b_j}}{x_{b_j}} = 0. \quad (47)$$

- du_m/dr is continuous at support radius $r = b_j$:

$$\Delta_j C_1 {x_{b_j}}^{m} + \Delta_j C_2(1+\nu) m(m-1) {x_{b_j}}^{m-2} - \Delta_j C_3 {x_{b_j}}^{-m} - \Delta_j C_4(1+\nu) m(m+1) {x_{b_j}}^{-m-2} + \Delta_j C_5(1+\nu) \left(\frac{bei_m' x_{b_j}}{x_{b_j}} - \frac{bei_m x_{b_j}}{{x_{b_j}}^2} \right) - \Delta_j C_6(1+\nu) \times \left(\frac{ber_m' x_{b_j}}{x_{b_j}} - \frac{ber_m x_{b_j}}{{x_{b_j}}^2} \right) + \Delta_j C_7(1+\nu) \times \left(\frac{kei_m' x_{b_j}}{x_{b_j}} - \frac{kei_m x_{b_j}}{{x_{b_j}}^2} \right) - \Delta_j C_8(1+\nu) \times \left(\frac{ker_m' x_{b_j}}{x_{b_j}} - \frac{ker_m x_{b_j}}{{x_{b_j}}^2} \right) = 0. \quad (48)$$

- The jump of the force Q_r owing to the presence of the force f_j at $r = b_j$ leads to the discontinuity equation

$$\lim_{r \to b_j^+} Q_r - \lim_{r \to b_j^-} Q_r = \frac{f_j}{2\pi b_j D} \exp(-im\theta_j), \quad (49)$$

which can be rewritten as

$$-\Delta_j C_5 bei_m' x_{b_j} + \Delta_j C_6 ber_m' x_{b_j} - \Delta_j C_6 bei_m' x_{b_j} + \Delta_j C_7 ber_m' x_{b_j} = -\frac{\tilde{f}_j l^3}{\pi b_j D}, \quad (50)$$

with

$$\tilde{f}_j = f_j \cos m\theta_j \text{ or } \tilde{f}_j = f_j \sin m\theta_j, \quad (51)$$

according to whether $w_m(r)\cos m\theta$ or $w_m(r)\sin m\theta$ is calculated, respectively. If several forces f_j are on the same radius b_j, we simply have

$$\tilde{f}_j = \sum_\alpha f_{j\alpha} \cos m\theta_{j\alpha} \text{ or } \tilde{f}_j = \sum_\alpha f_{j\alpha} \sin m\theta_{j\alpha}, \quad (52)$$

where α represents an arbitrary index of the forces at b_j.

It is possible to replace the four continuity equations at $r = b_j$ for v_m and u_m by four other equations: The continuity of v_m, N_r, $N_{r\theta}$, and N_θ or the continuity of v_m, ϵ_r, u_m, and du_m/dr, or also the continuity of v_m, du_m/dr, ϵ_r, and ϵ_θ, where N_θ is the direct stress resulting in the tangential direction, ϵ_r and ϵ_θ are the radial and the tangential deformation, respectively. These sets of equations lead to the same result. It is clear that the important point is to choose four linearly independent equations at $r = b_j$. Therefore one cannot combine ϵ_θ with w_m, ϵ_θ with v_m, ϵ_θ with u_m, or ϵ_r with dv_m/dr.

C. Harmonic $m = 1$

How does the previous set of equations change for $m = 1$? Johnson and Reissner[22] (see also Ref. 8) studied the free vibrations of thin shallow shells. They showed that no term in $1/r$ could exist in w_1 and also pointed out that the term in r in F_1 has no

physical sense. Therefore

$$m = 1 \Rightarrow C_2 = C_3 = 0. \quad (53)$$

It is easy to verify that C_2 is irrelevant in the expressions of N_r [Eq. (24)] and $N_{r\theta}$ [Eq. (25)]. The condition $C_3 = 0$ is obvious to avoid singularity in v_1 and u_1 (see Appendices A and B). The tilt term $C_1 x$ in w_1 characterizes only rigid-body displacement and can be omitted when the other C_i is calculated. The value of C_1 can be found *a posteriori* according to the condition that $w_1 = 0$ over the fixed points. The constant C_4 appears only in N_r and V_r, which must be zeroed at inner and outer edges, and is absent in equations to be solved at b_j.

Therefore, because the constants C_1, C_2, C_3, and C_4 are irrelevant at b_j, the number of equations at b_j decreases from $8k$ for $m > 1$ to $4k$ for $m = 1$. Note that the system of equations to be solved is thus slightly simpler than that given in Ref. 9.

Finally, the edge conditions Eqs. (29) and (30) become equal and show that, for $m = 1$, $N_r = N_{r\theta}$. Therefore one condition is lost at each edge.

Finally, the number of equations for harmonic $m = 1$ is thus $4k + 6$: $4k$ equations at b_j and six edge conditions. Their explicit forms are the following:

- Edge conditions: three equations at $r = c$ and three equations at $r = a$ [Eq. (22)].

The condition $N_r = N_{r\theta} = 0$ in $r = a$ leads to

$$aF_1'(a) - F_1(a) = 0 \quad (54)$$

or

$$-2C_4 x_a^{-1} + C_5(x_a bei_1' x_a - bei_1 x_a) - C_6(x_a ber_1' x_a - ber_1 x_a) + C_7(x_a kei_1' x_a - kei_1 x_a) - C_8(x_a ker_1' x_a - ker_1 x_a) = 0. \quad (55)$$

The two other edge conditions, $M_r = 0$ and $V_r = 0$ [Eq. (22)], are, respectively,

$$w_1''(a) + \frac{\nu}{a} w_1'(a) - \frac{\nu}{a^2} w_1(a) = 0, \quad (56)$$

$$-\frac{\partial \nabla^2 w_1}{\partial r} + (1-\nu)\left(\frac{w_1'}{r^2} - \frac{w_1}{r^3}\right) = 0, \quad (57)$$

or, respectively,

$$0 = C_5\left[-bei_1 x_a - (1-\nu)\left(\frac{ber_1' x_a}{x_a} - \frac{ber_1 x_a}{x_a^2}\right)\right] + C_6\left[ber_1 x_a - (1-\nu)\left(\frac{bei_1' x_a}{x_a} - \frac{bei_1 x_a}{x_a^2}\right)\right] + C_7\left[-kei_1 x_a - (1-\nu)\left(\frac{ker_1' x_a}{x_a} - \frac{ker_1 x_a}{x_a^2}\right)\right] + C_8\left[ker_1 x_a - (1-\nu)\left(\frac{kei_1' x_a}{x_a} - \frac{kei_1 x_a}{x_a^2}\right)\right], \quad (58)$$

$$0 = C_5\left[bei_1' x_a + (1-\nu)\left(\frac{ber_1' x_a}{x_a^2} - \frac{ber_1 x_a}{x_a^3}\right)\right] + C_6\left[-ber_1' x_a + (1-\nu)\left(\frac{bei_1' x_a}{x_a^2} - \frac{bei_1 x_a}{x_a^3}\right)\right] + C_7\left[kei_1' x_a + (1-\nu)\left(\frac{ker_1' x_a}{x_a^2} - \frac{ker_1 x_a}{x_a^3}\right)\right] + C_8\left[-ker_1' x_a + (1-\nu)\left(\frac{kei_1' x_a}{x_a^2} - \frac{kei_1 x_a}{x_a^3}\right)\right]. \quad (59)$$

- w_1 is continuous at $r = b_j$. Thus

$$\Delta_j C_5 ber_1 x_{b_j} + \Delta_j C_6 bei_1 x_{b_j} + \Delta_j C_7 ker_1 x_{b_j} + \Delta_j C_8 kei_1 x_{b_j} = 0. \quad (60)$$

- $\mathrm{d}w_1/\mathrm{d}r$ is continuous at $r = b_j$:

$$\Delta_j C_5 ber_1' x_{b_j} + \Delta_j C_6 bei_1' x_{b_j} + \Delta_j C_7 ker_1' x_{b_j} + \Delta_j C_8 kei_1' x_{b_j} = 0. \quad (61)$$

- $\mathrm{d}^2 w_1/\mathrm{d}r^2$ (or M_r) is continuous at $r = b_j$:

$$\Delta_j C_5 ber_1'' x_{b_j} + \Delta_j C_6 bei_1'' x_{b_j} + \Delta_j C_7 ker_1'' x_{b_j} + \Delta_j C_8 kei_1'' x_{b_j} = 0. \quad (62)$$

- The jump of the force Q_r owing to the presence of the force f_j at $r = b_j$ leads to the discontinuity equation:

$$\lim_{r \to b_j^+} Q_r - \lim_{r \to b_j^-} Q_r = \frac{f_j}{2\pi b_j D} \exp(-i\theta_j), \quad (63)$$

or

$$-\Delta_j C_5 bei_1' x_{b_j} + \Delta_j C_6 ber_1' x_{b_j} - \Delta_j C_6 bei_1' x_{b_j} + \Delta_j C_7 ber_1' x_{b_j} = -\frac{\tilde{f}_j l^3}{\pi b_j D}, \quad (64)$$

where $\tilde{f}_j$ is defined by Eq. (51).

It is possible to solve simultaneously, for a given $m \geq 1$, the set of $4(k+1) + 2$ (if $m = 1$) or $8(k+1)$ (if $m > 1$) equations to determine the C_i for all annular zones. But numerical methods, such as the Gauss–Jordan method, lower/upper triangular decomposition, or singular value decomposition,[23] involve a number of operations proportional to the power of 3 of the number of unknowns. Therefore, to save computer time, it is more efficient to solve the problem for 8 or 4 $\Delta_j C_i$ at each b_j and then to reconstruct C_i by using the edge conditions and $\Delta_j C_i$, as proposed by Menikoff for flat mirrors.[14]

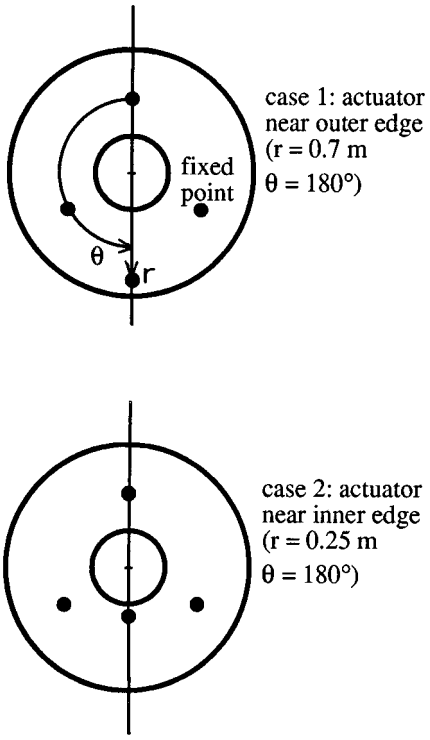

Fig. 2. Top view of the mirror with two different discrete force distributions. Forces are provided by three fixed points arranged with a threefold symmetry and an actuator near the outer edge (case 1, as in Fig. 1) or near inner edge (case 2).

5. Results and Discussion

To test the results above, an infinite radius of curvature (focal ratio, $F/ \sim 1000$) is considered first. In this case we observe that the deflections obtained by shallow shell theory converge perfectly toward the limit of the plate pure bending theory[13,14]: The differences are within 0.05%. This shows the robustness of the calculation in the limit case, $R = \infty$.

Deformations computed from the above theoretical results are shown in Fig. 3 for two different discrete force distributions (Fig. 2). It shows the difference between the AIF's for two distinct radii of curvature, $R = \infty$ and $R = 5.15$ m, in the case of the Optical Very Large Array[24,25] (OVLA) unit telescope primary mirror (Table 1). Quantitative data are given in Table 2.

Table 1. Characteristics of the OVLA Primary Mirror used in Fig. 3

Parameters	Values
Mirror outer radius a	0.760 m
Mirror inner radius c	0.175 m
Radius of curvature R	5.15 m
Focal ratio $R/4a$	1.69
Thickness h	24.0 mm
Young's modulus E	6.64×10^{10} Pa
Poisson's ratio ν	0.225
Specific mass	2500 kg. m^{-3}
Aspect ratio $h/2a$	1/63.3
Flexure ratio a^4/h^2	5.79×10^6 cm^2
Flexure ratio a^2/h^3	418 cm^{-1}

Table 2. Zernike Decomposition of the Deformations given in Fig. 3

Zernike Terms	Case 1, $R = \infty$ (nm)	Case 1, $R = 5.15$ m (nm)	Case 2, $R = \infty$ (nm)	Case 2, $R = 5.15$ m (nm)
Z_{11} (tilt)	591	565	145	143
Z_{20} (defocus)	74	17	−93	−20
Z_{22} (third-order astigmatism)	732	717	189	183

When the actuator acts near the mirror outer edge [Figs. 3(a) and 3(b)], it mainly excites the $m = 2$ harmonic (which is a kind of astigmatic deformation involving little stretching of the mirror middle surface) and is therefore hiding the stiffening effect from curvature on harmonic $m = 0$. But if the actuator acts near the central hole, on a radius smaller than that of the fixed points, Figs. 3(c) and 3(d) and Table 2 show that harmonic $m = 2$ is less excited, allowing one to see that harmonic $m = 0$ (mainly the defocus) is excited differently, depending on the R value. For a finite value of R the neutral plane is more noticeably stressed and the curvature stiffening effect is more visible because the defocused component (Table 2) is smaller.

The stiffening effect is more visible in Fig. 4 in which the GIF has been calculated for (a) $R = \infty$ and (b) $R = 5.15$ m for a three-point support at $b = 0.3820$ m. This support radius leads to the minimal rms deflection for $R = 5.15$ m. Obviously, this is no longer the case if $R = \infty$.

When must the shell theory be used instead of the simpler plate theory? The shell theory is indicated to obtain accurate mirror deformations for rotational symmetry, $m = 0$ and $m = 1$, because they always generate in-plane stresses.[8] Nevertheless the plate theory can be used with errors of less than ~5% according to the following rules of thumb:

$$\text{if} \quad \frac{R}{2a} \geq \sim 30 \quad \text{for } m = 0, \tag{65}$$

$$\text{if} \quad \frac{R}{2a} \geq \sim 10 \quad \text{for } m = 1. \tag{66}$$

For $m \geq 2$, Noethe[8] showed that the second natural mode of a given rotational symmetry m is affected most by the in-plane stresses. For example, to generate third-order astigmatism, $\propto r^2 \cos 2\theta$, close to the first natural mode with $m = 2$, the plate theory can be used with a loss of accuracy of only ~2% over a range of $\infty > R/2a \geq 2$. Only small in-plane stresses are generated by this kind of deformation. (No stretching of the mirror middle surface appears if the deformation is a developable surface; $r^2 \cos 2\theta$ defines the hyperbolic paraboloid, a ruled but not developable surface.[26]) But for fifth-order astigmatism, $\propto r^4 \cos 2\theta$, closer to the second natural mode with $m = 2$, the shell theory is indicated. The loss of accuracy with

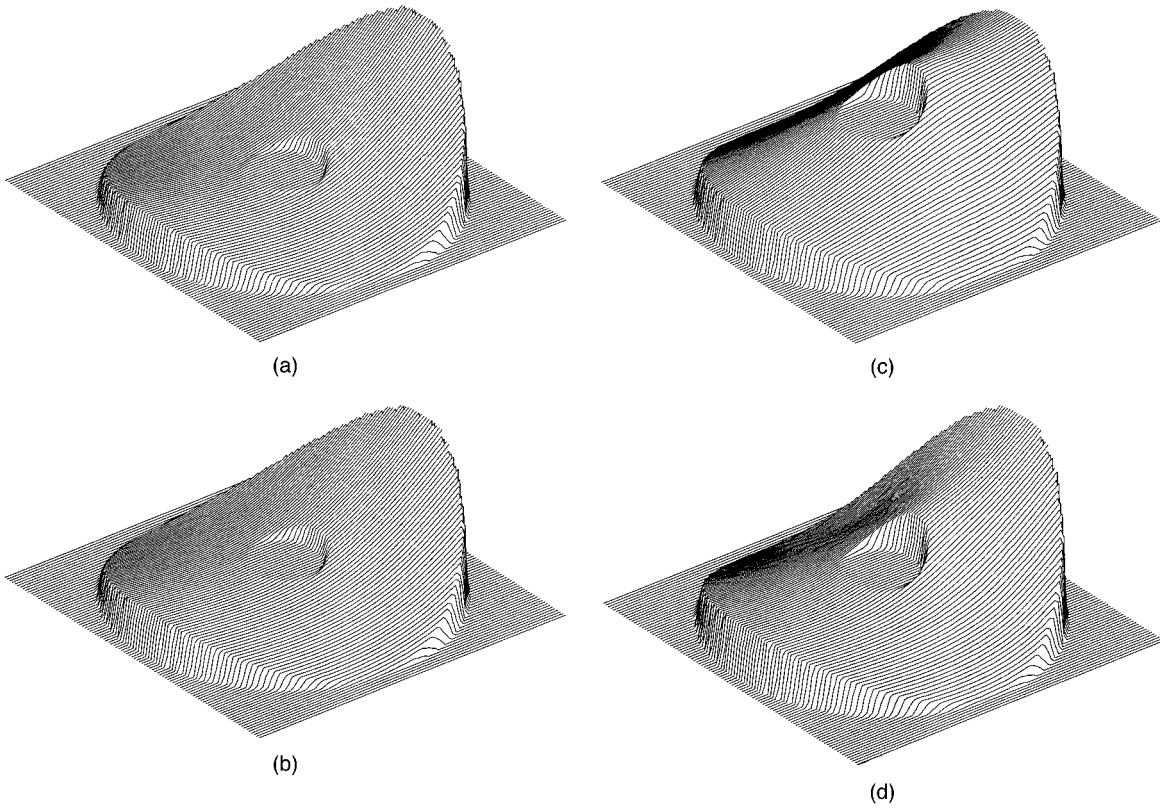

Fig. 3. Actuator influence functions of a meniscus-shaped mirror (Table 1). The mirror is supported by three fixed points and is under a fourth force applied by the actuator as in Figs. 1 and 2. Fixed points are at $r = 0.5084$ m. The actuator force, $f_4 = 1$ N, is upward. The series is truncated after the 15th nonzero term. (a), (b) Actuator at $b_4 = 0.7$ m, $\theta_4 = 180°$ (Fig. 2, case 1). (a) $R = \infty$, and the deformation is 2148-nm peak-to-valley (ptv), 438 nm rms. (b) $R = 5.15$ m, and the deformation becomes 2083 nm ptv, 421 nm rms. (c), (d) Actuator at $b_4 = 0.25$ m, $\theta_4 = 180°$ (Fig. 2, case 2). (c) $R = \infty$, and the deformation is 497 nm ptv, 124 nm rms. (d) $R = 5.15$ m, and the deformation becomes 496 nm ptv, 109 nm rms. The figures do not have the same vertical scale.

the plate theory is $\sim$20% at $R/2a = 2$, $\sim$5% at $R/2a = 4$ and $\sim$2% at $R/2a = 8$.

The analytical method (AM) is now compared with FEA results. The FEA code used here is Castem2000 developed by the Commissariat français à l'Energie Atomique. The mirror model features triangular thin-shell elements under pure bending.

Let us compare first the relative accuracy of the two methods. Table 3 shows the differences between the AIF's and the GIF and indicates that the two methods agree within 1%. This demonstrates now the robustness of the analytical calculation in the $R < \infty$ case.

Let us also compare the two methods in terms of the required computational resources. Table 4 gives quantitative data. Obviously the computing time increases linearly for the AM with the number of nodes on the mirror surface and with the number of terms in the Fourier series. This is no longer the case of the FEA, which involves a number of operations on a large matrix proportional to power 3 of the number of nodes.[23] As a consequence, the AM runs up to 30 times faster than the FEA. Note that if $R = \infty$, the plate theory can be used. Because the IF's then have a simpler polynomial form, one no longer needs to calculate the Kelvin functions, and computing time thus decreases by a further factor of $\sim$10.

Table 4 moreover shows that the AM requires typically 1000 times less memory than the FEA.

The AM is thus of particular interest when k AIF's are calculated simultaneously to fit a given Zernike or Seidel aberration present over the pupil and to be corrected; k being the number of actuators, the amplitude of each AIF is adjusted through a least-squares fit[23] to minimize the residual error between the target aberration and the combination of k AIF's.[7,9,13] Possibly we can reduce the number k by using any symmetry in the actuator configuration.

6. Conclusion

The purpose of this paper has been to give explicit sets of equations to be solved to calculate the IF's of a thin shallow meniscus-shaped mirror. The numerical results derived from the AIF Fourier series for a meniscus-shaped annular mirror of uniform thickness are in good agreement with the FEA results because the two techniques agree within 1%. The above theory can therefore be used with confidence to calculate the deformations of thin meniscus-shaped telescope mirrors.

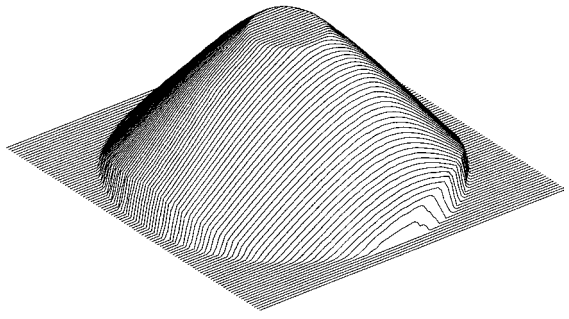

(a)

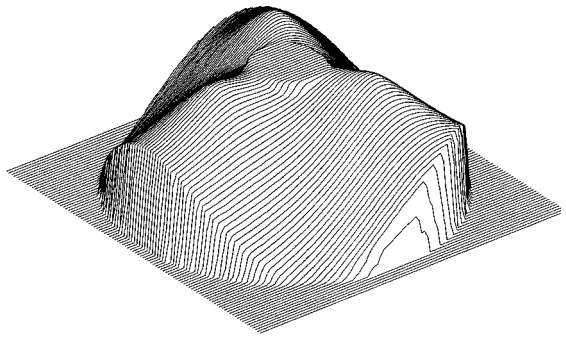

(b)

Fig. 4. Gravity influence functions of a meniscus-shaped mirror (Table 1). The mirror is supported by three points at $r = 0.3820$ m, which leads to the minimum rms deformation for $R = 5.15$ m. The series is truncated after the nonzero 15th term. (a) $R = \infty$, and the deformation is 134,377 nm ptv, 33,870 nm rms. (b) $R = 5.15$ m, and the deformation becomes 42713 nm ptv, 10,464 nm rms; (a) and (b) do not have the same vertical scale.

Table 3. Relative Accuracy of the Two Methods: Comparison between Deformations Computed by the FEA (w_{FEA}) and the AM (w_{AM}) for Computed AIF and GIF[a]

IF	$100 \times (w_{FEA} - w_{AM})/w_{FEA}$ Values (ptv)	$100 \times (w_{FEA} - w_{AM})/w_{FEA}$ rms (%) Values
AIF (Case 1)	0.033	0.83
AIF (Case 2)	−0.33	0.42
GIF	−0.67	−0.05

[a]The FEA model features triangular thin shell elements under pure bending. Each model features a number of nodes that are all on the mirror surface: 3685 nodes for the FEA model and the AIF; 2530 nodes for the FEA model and the GIF; 114,400 nodes for the AM model. The Fourier series was at least computed to the 15th nonzero term.

It has been pointed out that the calculation is much faster (30×) with the AM and requires much less memory (1000×). The AM technique thus allows rapid estimations of mirror deformations, which is convenient for active or passive mirror support optimization iterative processes[9,11,13] or parametric studies. Either large passive or active meniscus-shaped primary mirrors or Cassegrain/Gregorian adaptive secondaries can be considered.

Because the coming generation of large telescopes often involves segmented Keck-type mirrors,[27,28] this research should now be extended to hexagonal-shaped flat or curved mirror segments.

Appendix A: Expression of the Meridional Displacement *v*

The complete derivation of v_m was given by Berman.[5,9] Only the results needed to calculate the influence functions are given here. For $m = 0$ and $x = r/l$,

$$v_o(x) = -C_5 \frac{lx}{R} - \frac{(1+\nu)l}{R} \times \left(\frac{C_6}{x} + C_1 bei_0'x - C_2 ber_0'x + C_3 kei_0'x - C_4 ker_0'x \right), \tag{A1}$$

and for $m \geq 1$

$$v_m(x, \theta) = \frac{l \exp(im\theta)}{R} \left[\left(C_1 \frac{x^{m+1}}{m+1} + C_3 \frac{x^{-m+1}}{1-m} \right) - (1+\nu) \times (C_2 m x^{m-1} - C_4 m x^{-m-1} + C_5 bei_m'x - C_6 ber_m'x + C_7 kei_m'x - C_8 ker_m'x) \right]. \tag{A2}$$

Berman[5,9] showed that function $f = f(\theta)$ written as

$$f(\theta) = C_9 \exp i\theta + C_{10} \exp -i\theta \tag{A3}$$

must be added to v. But for load harmonics, $m \neq 1$, v cannot contain a term of symmetry of $m = 1$, and thus $C_9 = C_{10} = 0$. Note that C_3 must be zeroed in v_1 to avoid singularity.

Table 4. Comparison between FEA and AM in terms of Required Computational Resources[a]

Number of Nodes	Memory (Mbytes) for FEA	Memory (Mbytes) for AM	Ratio FEA/AM	CPU Times (s) for FEA	CPU Times (s) for AM	Ratio FEA/AM
361	5	0.0029	1720	12	18	0.7
700	11	0.0056	1960	33	20	1.6
1369	34	0.011	3090	97	21.5	4.5
2530	66	0.021	3140	470	22	21
3685	67	0.030	2230	761	23	33
4345	69	0.035	1970	905	24	37

[a]The computer used is a 9-Mflop workstation with 32 Mbytes of RAM and 100 Mbytes of swap memory. The Fourier series was computed to the 15th nonzero term. Mirror configuration, Case 1 (Fig. 2).

Appendix B: Expression of the Circumferential Displacement *u*

The complete derivation of u_m is given by Berman.[5,9] Only the results needed to calculate the influence functions are given here.

It is clear that $u_0 = 0$. For $m \geq 1$,

$$u_m(x, \theta) = -\frac{il \exp(im\theta)}{R}\left[C_1 \frac{x^{m+1}}{m+1} - C_3 \frac{x^{-m+1}}{1-m} + m(1+\nu) \times \left(C_2 x^{m-1} + C_4 x^{-m-1} + C_5 \frac{bei_m x}{x} - C_6 \frac{ber_m x}{x} + C_7 \frac{kei_m x}{x} - C_8 \frac{ker_m x}{x}\right)\right]. \quad \text{(B1)}$$

As for v, the function $f = f(\theta) = C_9 \exp i\theta + C_{10} \exp -i\theta$ must be added to u. But for load harmonics, $m \neq 1$, u cannot contain a term of symmetry of one, and thus $C_9 = C_{10} = 0$.

Note also that C_3 must again be zeroed in u_1, as in v_1, to avoid singularity.

My brother, G. Arnold, Ecole Normale Supérieure de Cachan, is gratefully acknowledged for many helpful discussions during this research and his valuable assistance in analyzing the mirror finite element model with Castem2000. The author thanks G. Lemaître, Observatoire de Marseille, for fruitful discussions and encouragement. Constructive comments by A. Menikoff, Itek, and L. Noethe, ESO, are gratefully acknowledged. The author especially thanks Robert Burnage, Observatoire de Haute Provence, who carefully read the manuscript. This research was supported by the Laboratoire d'Astrophysique Observationnelle, Collège de France, Paris.

References

1. O. C. Zienkiewicz, *The Finite Element Method in Engineering Science*, 2nd ed. (McGraw-Hill, London, 1971).
2. E. Reissner, "Stresses and small displacements of shallow spherical shells. I," J. Math. Phys. **25,** 80–85 (1946).
3. E. Reissner, "Stresses and small displacements of shallow spherical shells. II," J. Math. Phys. **25,** 279–300 (1947).
4. E. Reissner, "On the determination of stresses and displacements for unsymmetrical deformations of shallow spherical shells," J. Math. Phys. **35,** 16–35 (1959).
5. F. R. Berman, "Mathematical analysis of stress and displacement in thin shallow spherical shells," Ph.D. dissertation (Massachusetts Institute of Technology, Cambridge, Mass., 1946).
6. S. Timoshenko and S. Woinowsky-Krieger, *Theory of Plates and Shells* (McGraw-Hill, New York, 1959), Chap. 9, p. 282; Chap. 16, p. 558.
7. G. Schwesinger, "An analytical determination of the flexure of the 3.5-m primary and 1-m mirror of the ESO's New Technology Telescope for passive support and active control," J. Mod. Opt. **35,** 1117–1149 (1988).
8. L. Noethe, "Use of minimum-energy modes for modal-active optics corrections of thin meniscus mirrors," J. Mod. Opt. **38,** 1043–1066 (1991).
9. L. Arnold, "Petites déformations élastiques des plaques et des coques sphériques surbaissées: fonctions d'influence et application à l'optimisation de supports passifs ou actifs des miroirs minces de télescopes et aux miroirs adaptatifs," Ph.D. dissertation (Université de Nice Sophia Antipolis, France, 1995).
10. A. E. H. Love, *A treatise on the mathematical theory of elasticity*, 4th ed. (Dover, New York, 1944).
11. J. E. Nelson, J. Lubliner, and T. S. Mast, "Telescope mirror supports: plate deflection on point supports," in *Advanced Technology Optical Telescopes*, L. D. Barr and G. Burbridge, eds., Proc. SPIE **332,** 212–228 (1982).
12. P. K. Metha, "Non-FEM analysis and modeling in optostructural mechanics," in *Optomechanical Design*, P. R. Yoder, ed., Vol. CR 43 of SPIE Critical Reviews Series of Optical Science and Technology (SPIE, Bellingham, Wash., 1992), pp. 398–437.
13. L. Arnold, "Uniform load and actuator influence functions of a thin or thick annular mirror. Application to active mirror support optimization," Appl. Opt. **35,** 1095–1106 (1996).
14. A. Menikoff, "Actuator influence function of active mirrors," Appl. Opt. **30,** 833–838 (1991).
15. L. A. Selke, "Theoretical elastic deformations of solid and cored horizontal circular mirrors having a central hole on a ring support," Appl. Opt. **10,** 939–944 (1971).
16. D. S. Wan, J. R. P. Angel, and R. E. Parks, "Mirror deflection on multiple axial supports," Appl. Opt. **28,** 354–362 (1989).
17. E. Reissner, "The effect of transverse shear deformation on bending of elastic plates," J. Appl. Mech. **12,** A-69–A-77 (1945).
18. E. Reissner, "On bending of elastic plates," Q. Appl. Math. **5,** 55–68 (1947).
19. G. Lemaître, "Various aspects of active optics," in *Active Telescope Systems*, F. J. Roddier, ed., Proc. SPIE **1114,** 328–350 (1989).
20. M. Abramowitz and I. A. Stegun, *Handbook of Mathematical Functions* (Dover, New York, 1964), Chap. 9, p. 379.
21. G. Arfken, *Mathematical Methods for Physicists*, International ed. (Academic, New York, 1968), Chap. 8, p. 323; Chap. 16, p. 598.
22. M. W. Johnson and E. Reissner, "On transverse vibrations of shallow spherical shells," Q. Appl. Math. **15,** 367–380 (1958).
23. W. H. Press, S. A. Teukolsky, W. T. Vettering, and B. P. Flannery, *Numerical Recipes in C*, 2nd ed. (Cambridge U. Press, Cambridge, UK, 1992), Chap. 2, p. 32; Chap. 15, p. 671.
24. A. Labeyrie, C. Cazalé, S. Gong, F. Morand, D. Mourard, J. J. Kessis, J. P. Rambaut, F. Vakili, D. Vernet, and L. Arnold, "Construction of the Optical Very Large Array," in *Proceedings of ESO Conference on High-Resolution Imaging by Interferometry II*, J. M. Beckers and F. Merkle, eds. (European Southern Observatory, Garching-bei-München, Germany, 1991, 1992). pp. 765–773.
25. A. Labeyrie, D. Mourard, F. Morand, L. Arnold, B. Dejonghe, J. Dejonghe, C. Cazalé, G. Lemaître, D. Vernet, A. Blazit, J. Texereau, J. J. Kessis, J. P. Rambaut, "Progress on the optical very large array," in *Proceedings of the IAU Symposium on Very High Angular Resolution Imaging*, J. G. Robertson and W. J. Tango, eds. (SPIE, Bellingham, Wash., 1993; International Astronomical Union, Sydney, 1994), pp. 485–492.
26. K. A. Hirsch, ed., *Mathematics at a Glance, a Compendium* (VEB Bibliographisches Institut, Leipzig, 1975), Chap. 24, p. 545.
27. See papers of Session 2 in L. M. Stepp, ed., *Advanced Technology Optical Telescopes V*, Proc. SPIE **2199,** 82–141 (1994).
28. See papers of Session 2D, "Large telescopes: next step in collecting power," in *Proceedings of ESO/SPIE Symposium on Optical Telescopes of Today and Tomorrow*, A. Ardeberg, ed., 29 May – 2 June 1996, Landskrona/Hven, Sweden (SPIE, Bellingham, Wash., 1996).